A numerical simulation of VIV on a flexible circular cylinder

2012 Fluid Dyn. Res. 44 045508

(http://iopscience.iop.org/1873-7005/44/4/045508)

IOP PUBLISHING FLUID *DYNAMICS* RESEARCH

Fluid Dyn. Res. **44** (2012) 045508 (21pp) doi:10.1088/0169-5983/44/4/045508

A numerical simulation of VIV on a flexible circular cylinder

Fangfang Xie[1], Jian Deng[1,3], Qing Xiao[2] and Yao Zheng[1]

[1] School of Aeronautics and Astronautics, Zhejiang University, Hangzhou 310027, People's Republic of China
[2] Department of Naval Architecture and Marine Engineering, University of Strathclyde, Glasgow G4 0LZ, UK
E-mail: zjudengjian@zju.edu.cn

Received 18 July 2011, in final form 7 March 2012
Published 26 April 2012
Online at stacks.iop.org/FDR/44/045508

Communicated by H J Sung

Abstract

In this paper, numerical simulations of a flexible circular cylinder subjected to a vortex-induced vibration (VIV) are conducted. The Reynolds number for simulations is fixed at 1000. The finite volume method is applied for modeling fluid flow with the moving meshes feature. The dynamic response of a flexible cylinder fixed at both ends is modeled by the Euler–Bernoulli beam theory. The comparison between two-dimensional (2D) simulations and 3D simulations for the flexible cylinder shows that the maximum response amplitude of the cross-flow oscillation is about 0.57D for 2D rigid cylinders (modeled by a spring–damper–mass model) and 1.03D for flexible cylinders, respectively. The results from 3D simulations are closer to previous experimental results. Furthermore, the results obtained with various frequency ratios show that different wake patterns exist according to the frequency ratio, such as 2S mode, 2P mode and some more complicated modes. The wake pattern is different at various sections along the cylinder length, due to the fact that the two ends of the beam are fixed. The vibration of the flexible cylinder can also greatly alter the three dimensionality in the wake, which is our research in future work, especially in the transition region for Reynolds number ranging from 170 to 300.

(Some figures may appear in colour only in the online journal)

1. Introduction

Vortex-induced vibration (VIV) of solid structures has been known since ancient times, and remains a very important problem of fluid mechanics. The interest emanates primarily from its

---

[3] Author to whom any correspondence should be addressed.

0169-5983/12/045508+21$33.00

practical applications in a variety of engineering flows, such as transmission lines, suspension bridges and heat exchangers. Due to the complexity of the vortex dynamics associated with vortex shedding, a large number of studies have been carried out, as reviewed by Bearman (1984), Sarpkaya (2004) and Williamson and Govardhan (2004, 2008). Experimental studies of the VIV of circular cylinders, as well as some numerical investigations have provided many fundamental insights. Most of the previous studies are focused on fluid forces on a vibrating cylinder, vortex-shedding modes and synchronization regions for a freely vibrating cylinder, three dimensionality and free-surface effects, the frequency dependence of the added mass and the dynamics of cylinders with low mass damping. Moreover, aiming at studying the complicated nonlinear wake–body coupling characteristics in VIVs, semi-empirical models such as wake-oscillator models have been developed, and some advanced numerical methods have been developed and applied to solve the fully coupled VIV (Gabbai and Benaroya (2005)).

Researchers are seeking a combined parameter, like S_G or $m^{**}\xi$, as a universal parameter to couple the effects of both mass and damping on the dynamic response of the cylinder in the VIV problem. Depending on mass-damping ($m^{**}\zeta$), it is well known that there exist two types of amplitude response between the maximum response amplitudes $A_{\max}$ and the reduced velocity U^*. At a high mass-damping, Feng (1968) showed that there are two amplitude branches, namely the 'initial' branch and the 'lower' branch, with a hysteretic transition between the two branches. The jump in response amplitude is reflected by a significant jump in the phase of the pressure fluctuations relative to body motion and the phase jump corresponds to a change in the wake patterns, from 2S to 2P (Willamson 1988). However, at low mass-damping (Khalak and Williamson 1996, 1997a, 1997b, 1999; Govardhan and Williamson 2000), it is associated with the existence of an upper branch of high amplitude response, which appears between the initial and lower branches. The frequency of the lower branch is not close to the cylinder natural frequency. Reducing mass leads to a significant increase of the lock-in regime. In addition, it is found that the response branch relates to the wake vortex-shedding mode. Within the initial branch, a single vortex is shed in each half cycle of oscillation as the 2S mode. At the upper branch, two vortices are shed in each half cycle of oscillation, which makes it compatible with the 2P mode, but the second vortex of each pair is much weaker than the first one. At the lower branch, two vortices are shed in each half cycle of oscillation as the 2P mode. It should be noted that most of the above results are obtained with a 2D and rigid hypothesis of the cylinder, or the dynamic spring–damping–mass system of the cylinder.

With increasing demands for a more comprehensive understanding of VIV in realistic engineering problems, studies on the VIV problem have been expanded into 3D and flexible cylinders during recent years. Deng *et al*'s (2007) numerical investigations provided details on the wake characteristics associated with two circular cylinders arranged perpendicular to each other in a uniform flow field. They found that the peak amplitude of vibrations for the cruciform arrangement is lower than that for an isolated cylinder, and the resonance region is wider than that of an isolated cylinder. A distinct vortex-shedding pattern in the wake is studied as well. Moreover, the flexible cylinder supporting is another important factor that affects the coupled flow-structural characteristics. For a flexible cylinder VIV, the cable-like and beam-like structures are two generally accepted structural systems. If the tension dominates, it is termed a cable, while if the bending rigidity dominates, it is termed a beam. Results from Lee and Allen (2010) show that the vibration frequency of a cylinder rises with the flow speed for a tension-dominated structure but does not rise significantly for a bending rigidity controlled structure. In addition, the lock-in bandwidth is broad with rigidity controlled cases, indicating a weak linkage between the variation of vibration frequency and the lock-in bandwidth.

In previous studies, the predictions of VIV for a tension-dominated cable have been extensively conducted both experimentally and computationally. By using direct numerical simulations, Newman and Karniadakis (1996, 1997) investigated the flow-induced vibration of an infinitely long flexible cable. By comparing the forced cable with the VIV cables, they found that the responses are different, and the divergence increases at high Reynolds numbers. Evangelinos and Karniadakis (1999) also presented the direct numerical simulation results of a vibrating rigid cylinder, a cable, and a beam at a Reynolds number of 1000. They found mixed shedding patterns of 2S, 2P and P + S in the wake, and the amplitude of the cylinder vibrating is around 1D, higher than that of the laminar cases (0.5D–0.6D). Huera-Huarte and Bearman (2009a, 2009b) indicated that when the lowest tension is imposed on the model, its dynamic response is very similar to that of a rigid cylinder, which could be clearly defined as initial, lower and upper branches of response. As the tension is increased, it starts to behave like a cable or a tension dominated structure. The lower branch disappears; thus all responses are concentrated within the initial and upper branches. Furthermore, the vortex modes in the wake of the oscillating cylinder are found to be dependent on the amplitude distribution along the length of the model. Xu *et al* (2009) revealed that within the range of Reynolds numbers, the vibration frequencies and amplitude to diameter ratios of the riser tested, three vortex modes 2S, 2P and P + S formed in the near wake of the riser. The vortex-shedding modes depend on the Reynolds number, the vibration frequencies, and the amplitude to cylinder diameter ratio.

Studies on bending stiffness dominated problems have also attracted much attention. Experimentally, Brika and Laneville (1993, 1995, 1996) provided evidence of 2P to 2S mode transition with a free vibrating flexible circular cylinder in its transversal direction. It was observed that each branch of the loop was associated with a vortex-shedding mode. With a flexible cantilever, Pesce and Fujarra (2000) and Fujarra *et al* (2001) observed a hysteretic transition of amplitude response from an initial branch to a lower branch that is similar to the elastically mounted or free oscillating cylinder. From the numerical simulation aspect, the Euler–Bernoulli beam theory is extensively applied by many researchers. Meneghini *et al* (2004) and Yamamoto *et al* (2004) applied the 2D discrete vortex method (DVM) to visualize the vortex structure in the wake of a flexible vibrating cylinder. A 2S mode was found associated with low amplitudes; it is changed to a 2P mode with large amplitudes. The transition point varies with the reduced velocity. Huera-Huarte *et al* (2006) used a finite-element method to investigate the force distribution along a flexible circular cylinder. Huang *et al* (2010) studied long riser VIV in uniform/sheared currents using the time-domain numerical simulation approach and found that the vortex-shedding pattern is mainly the 2S type while its appearance varies significantly with different elevations along the risers.

As reviewed above, a few studies have been conducted to explore the flow mechanism associated with flexible cylinder VIV. Limited studies on flexible cylinders are focused on the vibrating response rather than the flow characteristic in the oscillating cylinder. In the present study, a numerical study on a flexible cylinder VIV is carried out at a Reynolds number of 1000. Apart from detailed discussion on the structural parameter influence on the dynamic response of the flexible cylinder, the wake vortex structures will be fully investigated. To simply the problem, the mass ratio of the cylinder is fixed as 10 and the dominant motion is assumed in the cross-flow direction. To obtain different responses of the coupled flow–structure system, we vary the structure's bending stiffness to model the behavior of a fixed–fixed flexible cylinder. Although the above limitations exist in the present study, we believe that there will be some qualitative results, and these will provide new insights into

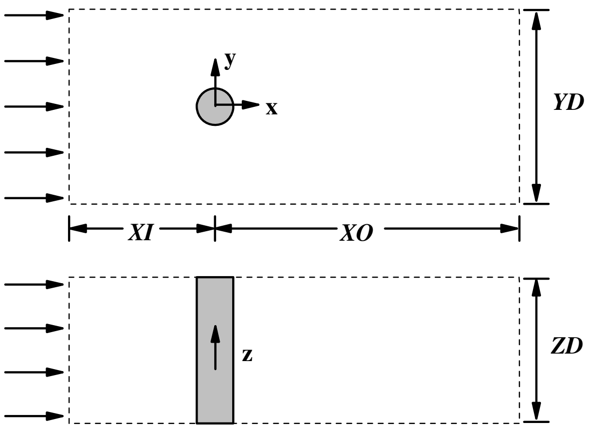

Figure 1. Geometrical model and computational domain.

the mechanism of the flexible vortex vibrating cylinder. The paper is organized as follows. First the physical models, the fluid solver, the structure solver and the coupling method are introduced; then the numerical results of the VIV for a rigid and flexible cylinder are both presented and discussed. Conclusions are drawn in the final section.

2. Physical models and numerical methods

2.1. Computational domain and boundary conditions

In this paper, a cuboids flow field is considered, and the detailed geometry configuration is depicted in figure 1. Here, XI (12D) and XO (25D) are distances from the inlet and outlet relative to the cylinder center. YD (16D) and ZD (12D) denote the lateral and span-wise dimensions of the computational domain, respectively.

The boundary conditions employed for the present investigation are specified below. At the inlet, a constant stream-wise velocity is imposed with other velocities set to zero, and the nonreflecting boundary condition is imposed at the outlet. At the cylinder wall, the impermeability and no-slip condition is applied for velocity. In order to simulate an infinite long cylinder, the free-slip conditions are imposed at both the transverse and span-wise computational boundaries. The pressure Neumann condition is applied to the inlet, surface of the cylinder and the pressure Dirichlet boundary condition is applied to the outlet boundary.

The mesh is non-uniform at the x–y plane but uniform in the z-direction. The grid is clustered near the cylinder and the spacing is increased with the distance increasing away from the cylinder surface. The first grid size near the cylinder is set to 0.01D, and the time step is 0.005 according to the Courant–Friedrichs–Lewy (CFL) condition.

2.2. Finite-volume method on moving meshes

The fluid flows are solved using the finite-volume method with moving meshes (Batina 1990; Ferziger and Peric 1995). The moving finite-volume cells must be adjusted to the time-varying shape of the interface. The Laplace equation-based (Jasak and Tukovic 2007) deforming mesh approach is used in this study where the internal control-volume (CV) vertices are moved based on a prescribed motion of the boundary vertices while the topology of the mesh remains unchanged. The displacement equation (Laplace equation) for mesh moving is discretized at the vertices of the finite-volume mesh and solved by the finite-element method.

An incompressible Newtonian fluid is assumed, for which the integral form of the governing equations with moving meshes is given by

$$\frac{\mathrm{d}}{\mathrm{d}t}\int_{V_{\mathrm{P}}}\mathrm{d}V+\int_{V_{\mathrm{P}}}\nabla\cdot(U-U_b)\,\mathrm{d}V=0, \tag{1}$$

$$\int_t^{t+\Delta t}\left[\frac{\partial}{\partial t}\int_{V_{\mathrm{P}}}U\mathrm{d}V+\int_{V_{\mathrm{P}}}\nabla\cdot((U-U_b)U)\,\mathrm{d}V-\int_{V_{\mathrm{P}}}\nabla\cdot(\nu\nabla U)\,\mathrm{d}V\right]\mathrm{d}t$$
$$=-\int_t^{t+\Delta t}\left(\int_{V_{\mathrm{P}}}\nabla p\,\mathrm{d}V\right)\mathrm{d}t, \tag{2}$$

where U is the fluid velocity, U_{b} is the boundary velocity, the subscript P represents the cell values, and V_{P} is the cell volume. As the volume V_{P} is no longer fixed in space, its motion is captured by the motion of its bounding surface S by the velocity U_{b}.

The method is based on discretizing the integral form of governing equations over an arbitrary moving volume V. After the general form of Gauss's theorem is applied and the second-order finite-volume discretization is used, equation (2) is transformed into sums of face integrals and approximated to second order using the mid-point rule.

$$\frac{3(U_{\mathrm{P}}V_{\mathrm{P}})^n-4(U_{\mathrm{P}}V_{\mathrm{P}})^o+(U_{\mathrm{P}}V_{\mathrm{P}})^{oo}}{\mathrm{d}t}+\sum_f(F-F_S)U_f-\sum_f\nu_f S\cdot(\nabla U)_f=-(\nabla p)V_{\mathrm{P}}, \tag{3}$$

where $(U_{\mathrm{P}}V_{\mathrm{P}})^n=(U_{\mathrm{P}}V_{\mathrm{P}})(t^o+\delta t)$, $(U_{\mathrm{P}}V_{\mathrm{P}})^o=(U_{\mathrm{P}}V_{\mathrm{P}})(t^o)$, $(U_{\mathrm{P}}V_{\mathrm{P}})^{oo}=(U_{\mathrm{P}}V_{\mathrm{P}})(t^o-\delta t)$, $F=S\cdot U_f$ is the fluid flux, F_S is the mesh motion flux and f is the face value. However, the fluid flux F is usually obtained as a part of the solution algorithm and satisfies the conservation requirements. The face-center values of all dependent variables are calculated using linear interpolation of the neighboring cell-center values. The second-order upwind spatial discretization scheme is applied to the convective term and the second-order central differencing corrected scheme is used for the viscous term. The temporal discretization of all equations is performed by using the second-order accurate implicit three-time-level scheme as the backward scheme. One can refer to Ferziger and Peric (1995) for details of this finite-volume method.

The relationship between the rate of change of the volume V and the velocity U_{b} is defined by the so-called space conservation law (SCL) (Demirdzic and Peric 1988).

$$\frac{\mathrm{d}}{\mathrm{d}t}\int_{V_{\mathrm{P}}}\mathrm{d}V+\int_{V_{\mathrm{P}}}\nabla\cdot U_{\mathrm{b}}\mathrm{d}V=0. \tag{4}$$

The discretized counterpart of the SCL where the backward scheme is used for temporal discretization reads

$$\frac{3V_{\mathrm{P}}^n-4V_{\mathrm{P}}^o+V_{\mathrm{P}}^{oo}}{\Delta t}-\sum_f F_S=0. \tag{5}$$

The mesh flux F_S is calculated as the volume swept by the face f in motion during the current time-step rather than from the grid velocity U_{b}, making it consistent with the cell volume calculation.

It is noted that the discretized form of momentum equation (3) can be transformed into the form of a linear algebraic equation, which can be solved using the geometric agglomerated algebraic multi-grid solver. The pressure is solved from the pressure Poisson equation, which is derived by applying the divergence operator to the momentum equations and discretized by a second-order central difference scheme, and then a Gauss Seidel iteration method is applied to solve it. In this study, the Pressure Implicit with Splitting of Operators (PISO) procedure proposed by Issa (1986) is used for dealing with the pressure–velocity coupling. The discretized mesh motion equation governed by a Laplacian as described before is diagonally dominant, allowing the use of the Incomplete Cholesky preconditioned Conjugate Gradient (ICCG) iterative solver.

2.3. Cylinder motion equation

To validate the fluid solver involving a moving mesh, we firstly study a 2D rigid cylinder freely oscillating in transverse directions. After that, a flexible 3D cylinder is investigated and the interactions between the cylinder and its surrounding fluid are numerically examined. In this section, the governing equations of the cylinder in both cases are introduced.

2.3.1. Two-dimensional spring–damper–mass model. The transverse displacement of the cylinder, $y(t)$, due to the fluid force is modeled using a spring–damper–mass model. Thus, the cylinder's transverse motion equation is given by

$$m\ddot{y}+c\dot{y}+ky = F_y, \tag{6}$$

where m is the cylinder mass, c is the damping coefficient and k is the structural stiffness. The second-order Lax–Wendroff method is used to compute the position of the cylinder and the Euler explicit method is adopted to predict the body velocity, as shown below:

$$y^{n+1} = y^n+\dot{y}^n\Delta t+\frac{1}{2}\ddot{y}^n\Delta t^2, \tag{7}$$

$$\dot{y}^{n+1} = \dot{y}^n+\ddot{y}^n\Delta t, \tag{8}$$

where

$$\ddot{y}^n = \frac{F_y}{m} - \frac{c}{m}\dot{y}^n - \frac{k}{m}y^n. \tag{9}$$

2.3.2. Dynamic equation for a 3D flexible cylinder. To simplify the problem, the vibration of a flexible cylinder with its two span-wise ends being fixed is modeled by the Euler–Bernoulli beam theory. Thus the damping and tension characteristics along the beam are not considered. Only the cylinder blending at cross-flow direction is included, which is given by

$$\rho_l\frac{\partial^2 y(z,t)}{\partial t^2}+EI\frac{\partial^4 y(z,t)}{\partial z^4} = f(z,t). \tag{10}$$

The cylinder is fixed at both ends; therefore the boundary condition is specified as

$$y(0,t)=0,\ y(l,t)=0,\quad \frac{\partial y(0,t)}{\partial z}=0,\quad \frac{\partial y(l,t)}{\partial z}=0, \tag{11}$$

where ρ_l is the mass per unit length of the cylinder, EI is the stiffness, l is the length of the cylinder, and $f(z,t)$ is the distributed lift force on the cylinder.

The finite-difference method is utilized to discretize the beam equation. The central difference scheme with lagged approximation of the first derivative is used because of its popularity in structural dynamics. The finite-difference beam equation of the ith node is represented as

$$\frac{\partial^2 y_i}{\partial t^2} = \frac{f_i}{\rho_l} - \frac{EI}{\rho_l}\frac{y_{i+2}-4y_{i+1}+6y_i-4y_{i-1}+y_{i-2}}{\Delta z^4}, \tag{12}$$

where y_i is the displacement at the ith node, and Δz is the finite-difference grid size ($\Delta z = l/n$), where n is the number of elements or segments along the span-wise direction.

The boundary condition is imposed by the central difference method with two additional virtual nodes at $i = -1,\ i = n+1$. Note that the physical boundary conditions at the fixed ends are described as zero displacement and zero gradient, respectively:

$$y_0 = 0, \quad y_{n+1} = 0, \quad y_{-1} = y_2, \quad y_{n-1} = y_{n+1}. \tag{13}$$

The influence of the number of elements on the solution and the verification of numerical schemes for the structure model are considered. The free vibration of the two ends fixed beam is studied. The frequency equation is expressed as

$$\cos\lambda\ \cosh\lambda - 1 = 0. \tag{14}$$

The first, second and third roots of the above equation are 4.73, 7.854 and 10.996. For $i \geqslant 3$, equation (14) can be simplified as $\cos\lambda - 1 = 0$; thus the root of the equation is $\lambda_i = (i+1/2)\pi$. The corresponding nth eigenfrequency is

$$\omega_i = (\lambda_i)^2 \sqrt{\frac{EI}{\rho_l l^4}}. \tag{15}$$

The nth eigenfunction $\phi_i(x)$ is presented as

$$\phi_i(x) = \cos\beta_i x - \cosh\beta_i x + \eta_i(\sin\beta_i x - \sinh\beta_i x), \tag{16}$$

where $\beta_i = \lambda_i/l$ and where η_i is defined as

$$\eta_i = -\frac{\cos\beta_i l - \cosh\beta_i l}{\sin\beta_i l - \sinh\beta_i l}. \tag{17}$$

We select the first eigen-frequency to be approximately equal to $2\pi f_o$, where f_o is the natural vortex-shedding frequency of the flow around a rigid cylinder at $Re = 1000$. Based on that, the modulus of elasticity and first eigen-mode can be theoretically calculated. With the first eigen-mode employed as the cylinder's initial deformation, three cases with various N as 6, 12 and 24 are compared. The vertical displacements of each center point are shown in figure 2 along with corresponding oscillating frequencies. The predicted oscillating frequencies are 0.201, 0.211 and 0.22, respectively. Compared with the assumed first eigen-frequency, the errors of those computed frequencies are 8.65, 4.09 and 0% for $N = 6$, 12 and 24, respectively. To save computational time and satisfy certain convergent and accurate requirements, it is recommended that $n = 12$ is the best choice in this case. However, it should be pointed out that flow is solved with $N = 36$ points in the span-wise direction, which is different from the segments used for the structural solver. Such mesh points are fine enough to capture the 3D flow characteristics of a cylinder. With all finite-difference equations established for all nodes, the fixed–fixed beam system can be solved by using the Runge–Kutta algorithm for the internal nodes ($i = 1 \sim n - 1$) along with the specified boundary conditions. The node displacement and velocity are updated at each time step.

2.4. Fluid–structure coupling method

The loosely coupled method (Schulz and Kallinderis (1998)) is utilized between the fluid and the structural solvers. In figure 3, a schematic view of the coupling process is given. After initialization, the flow field is firstly solved using the computational fluid dynamics (CFD) flow solver. The fluid forces on the cylinder surface are computed, which are passed to the CSD structural solver to determine the deformation of the cylinder wall. The CFD mesh is then

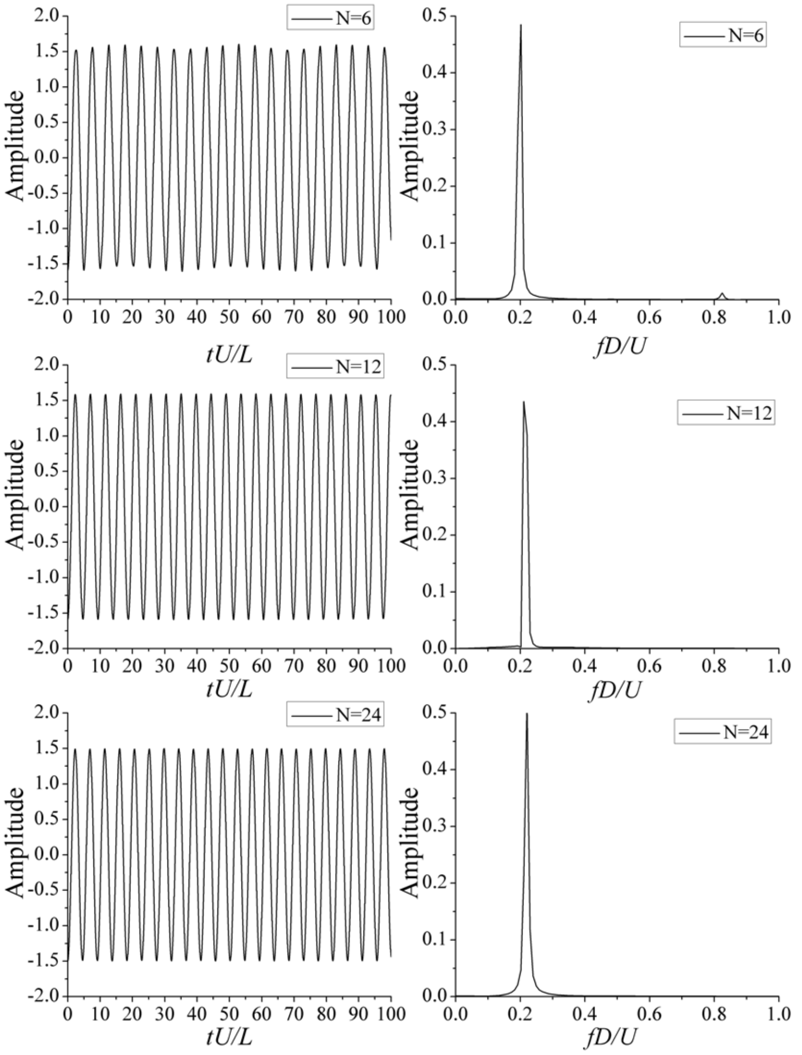

Figure 2. Vertical displacements of the center points and their corresponding frequency for different cases.

updated according to the latest CSD mesh. Such a fluid–structure interaction (FSI) iteration loop is repeated during each time step for this unsteady problem. Various tests have shown that they will converge to the final solution when the time step is smaller than 0.005 s in the present study.

3. Results and discussion

In this section, the computed results for a 2D rigid cylinder VIV will be firstly presented, in which the dynamic response associated with different frequency ratios, the beating behavior and the lock-in phenomenon will be compared with available published data. Next, we will focus on a 3D flexible cylinder simulation. The results will include the comparison with a rigid

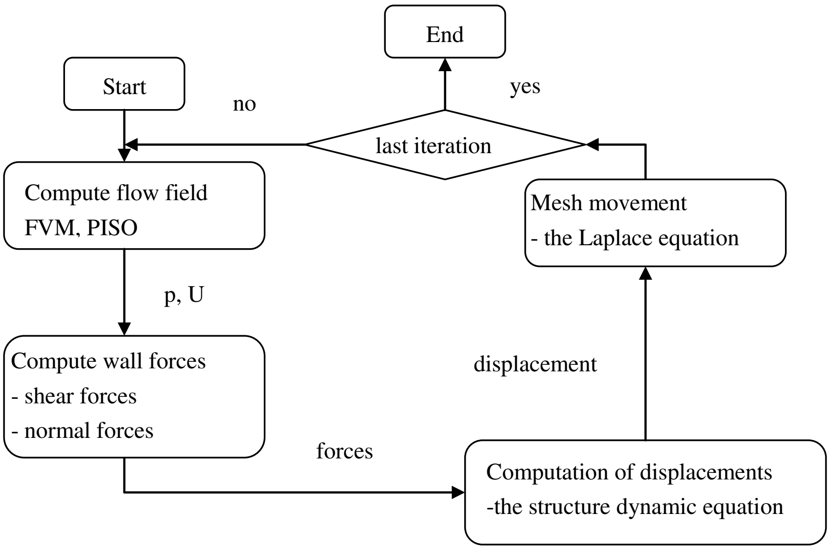

Figure 3. Flow chart of coupled solution procedure.

Table 1. Maximum response amplitude of the vibrating circular cylinder.

Reference	Methods	$m^*\xi$	A (peak)
Griffin (1992)	Experiment	–	1.0
Evangelinos and Karniadakis (1999)	3D Code (DNS)	0.00	0.74
Evangelinos and Karniadakis (1999)	2-D Code (DNS)	0.00	0.55
Schulz and Kallinderis (1998)	2D Code (RANS)	0.013	0.67
Present study	2D code (Laminar)	0.013	0.56
Present study	2D code (Laminar)	0.00	0.57

cylinder and investigation on the contribution of frequency ratio to the dynamic response of the cylinder and vortex patterns in the wake.

3.1. Two-dimensional rigid cylinder VIV

While it is not the main focus of this study, the 2D simulation of the VIV for a rigid cylinder at different frequency ratios is studied first as a basis for comparison with other numerical and experimental results. In our previous studies, a finite-difference method based solver as well as an immersed-boundary method based solver have been implemented in the simulations of VIV for both 2D and 3D cylinders (Deng *et al* (2005), Deng *et al* (2007)). In the present study, a finite-volume method based solver is used; detailed code verification is therefore carried out.

By using a one degree-of-freedom structure model (spring–damper–mass model), the VIV for a rigid cylinder is simulated. The current simulations are compared with other computational and experimental results, as shown in table 1, in which all numerical and experimental results are obtained at $Re = 1000$. Compared to the numerical results by the 2D DNS code by Evangelinos and Karniadakis (1999), the present results show good agreement in terms of the maximum response amplitude with and without damping. However, the response amplitude is lower than that of the 3D DNS result by Evangelinos and Karniadakis (1999), and the 2D RANS result by Schulz and Kallinderis (1998). It is due to the unsolved three-dimensionality turbulence influence in the present 2D study. Furthermore, this difference highlights the necessity of implementing 3D studies.

Figure 4 shows force coefficients and displacement time histories at different frequency ratios ($f_\mathrm{n}/f_\mathrm{o}$) with a mass-damping ratio of 0.0013, where f_n is the natural frequency of the cylinder and f_o is the vortex-shedding frequency for a rigid cylinder. The beating behavior can be clearly observed in figure 4(a) and at the initial stage in figure 4(b). For $f_\mathrm{n}/f_\mathrm{o} = 1.08$, the response behavior changes to another state, in which the response amplitude reaches a value of 0.53. Over the region of $f_\mathrm{n}/f_\mathrm{o} = 1.06 - 0.89$, it is noted that the cylinder vibrates at a certain frequency and in a narrow range of response amplitudes, indicating that the vortex-shedding frequency is fully locked on to f_o. In the lock-in region, the response amplitudes vary in a small range of 0.52–0.56. For $f_\mathrm{n}/f_\mathrm{o} = 0.82$, the response amplitude falls to a small value and the system is unlocked.

Instantaneous vorticity fields in the wake of an oscillating cylinder at various frequency ratios are shown in figure 5. At low transverse oscillating amplitude, the classical Kármán shedding (2S) is observed. Once the cylinder response jumps to a large amplitude, it is associated with the C(2S) mode of vortex shedding. The C(2S) mode is very similar to the 2S mode except that the vortices coalesce in the far wake. This can be obviously seen, for example, at $f_\mathrm{n}/f_\mathrm{o} = 1.08$, at which point the vortex-shedding frequency approximately matches the natural frequency of the cylinder. The transverse spacing of the vortex street for 2S and C(2S) modes is slightly different. In the lock-in region, the width of the street becomes large as the frequency ratio increases and then becomes small with further increase of frequency ratio. This is because the branch switches from the initial branch to the lower branch. When the amplitude reaches the maximum value at a frequency ratio of 0.89, a $\mathrm{P}+\mathrm{S}$ mode with one vortex pair and one single per cycle can be seen in the near wake, and an irregular vortex mode forms in the far wake. The frequency ratio, $f_\mathrm{n}/f_\mathrm{o} = 0.82$, marks the end of the synchronization, and the vortex mode returns to the 2S mode for a rigid cylinder.

3.2. Three-dimensional flexible cylinder VIV

3.2.1. Comparison with a rigid cylinder. In order to understand well the dynamic response of a flexible cylinder, 3D simulations of the flow past a rigid circular cylinder and a flexible cylinder at a specific frequency ratio of $f_\mathrm{n}/f_\mathrm{o} = 0.9$ are carried out for comparison, where f_n is the first eigen-frequency of a flexible cylinder at the specified modulus elasticity. It should be noted that the dynamic response of this cylinder is governed by simplified Euler–Bernoulli beam theory, with only the cross-flow direction motion being allowed.

Compared to the rigid cylinder, the flexible cylinder shows its shape deformation due to the unsteady forces related to vortex shedding. Five sections of the cylinder along the span-wise direction are picked out for comparison. They are $z/D = 2$, 4, 6, 8 and 10. In figure 6 the instantaneous cross-flow displacements and the spectral analysis of the displacement are shown. At all sections, a clear single peak can be identified and they turn out to be the same as the excited structural frequency of $f = 0.195$. Figure 6(c) shows the cross-flow motion every (1/10)th of a period, where a clear first mode presented by a half period of sinusoidal mode shape is observed.

In this paper, a Lambda-definition from Jeong and Hussain (1995) is introduced to identify the core region of the vortex. In figure 7, 3D vortex structures are shown for two cases: (a) the wake of the rigid cylinder maintains the primary Kármán vortex and a small quantity of stream-wise vortex pairs; (b) the wake along the span-wise direction of the flexible cylinder is disordered. The vortex structures exhibit much more 3D instability. It should be noted that the differences of three dimensionality between rigid and flexible cylinders can only be roughly

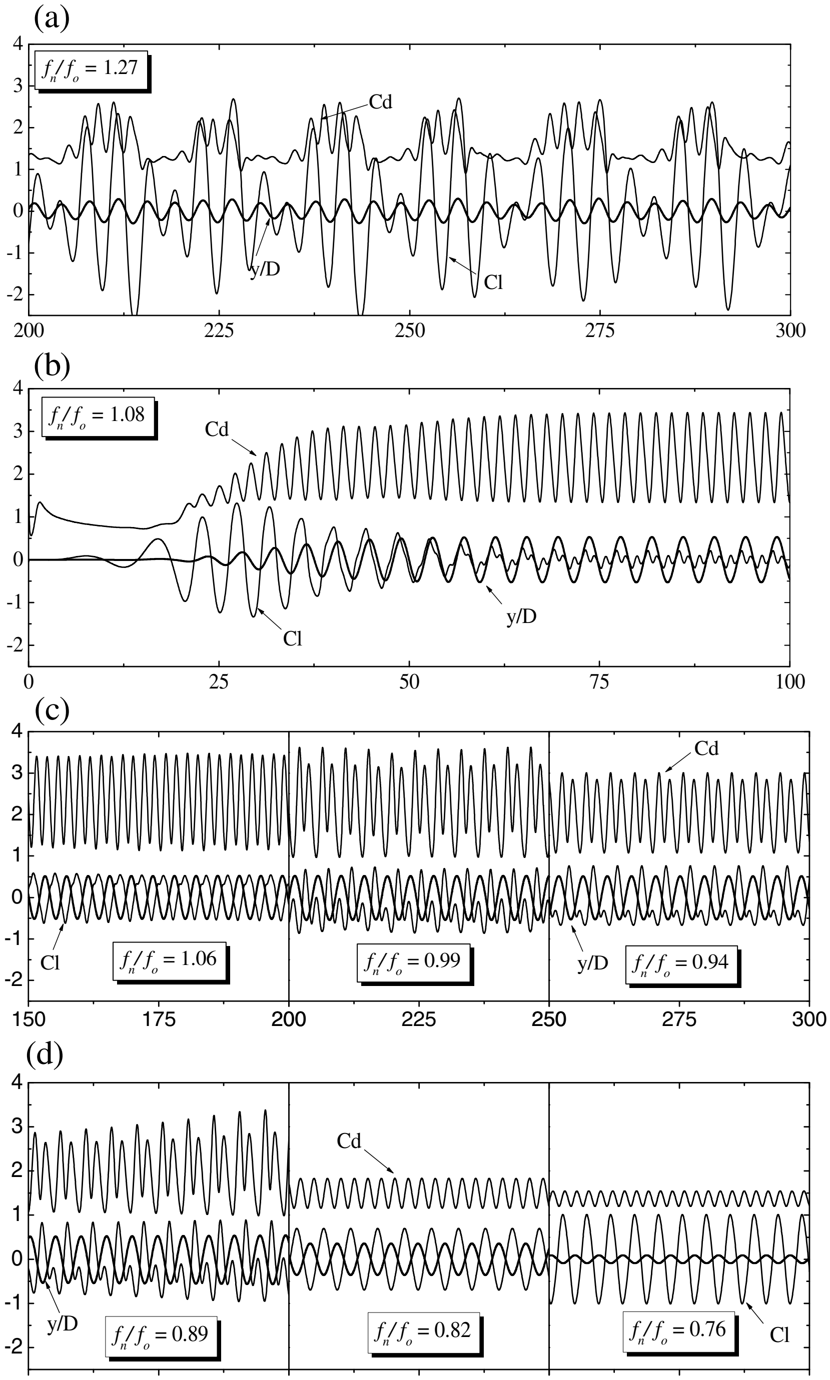

Figure 4. Force coefficients and displacement time histories at different frequency ratios.

compared, due to the poor resolution along the span-wise direction of the cylinder. With a closer observation, different vortex structures at five different sections along the cylinder are presented in figure 8. Due to the vibrating movement of the flexible cylinder, the wake patterns

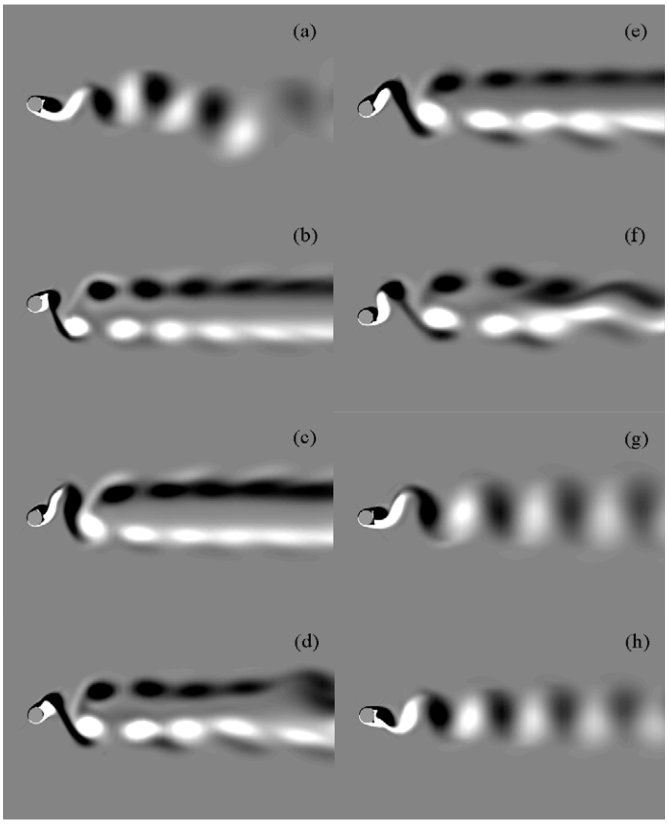

Figure 5. Instantaneous vorticity contours at various frequency ratios (a) $f_n/f_o = 1.27$, (b) $\mathrm{f_n}/f_o = 1.08$, (c) $\mathrm{f_n}/f_o = 1.086$, (d) $\mathrm{f_n}/f_o = 0.99$ (e) $\mathrm{f_n}/f_o = 0.94$, (f) $\mathrm{f_n}/f_o = 0.89$, (g) $f_n/f_o = 0.82$ and (h) $\mathrm{f_n}/f_o = 0.76$.

are expected to vary in different sections along the length. The same characteristic has also been observed by previous experimental studies of Flemming and Williamson (2005) and Huera-Huarte and Bearman (2009b).We can figure out that: (a) In the wake of the flow of a rigid cylinder, the main vortex structure is the classical vortex street, with two single vortices per cycle or 2S patterns at different span-wise positions. (b) In the wake of a flexible cylinder, the flow structures are more complicated. A 2P mode with two vortex pairs per cycle can be seen in the wake of the vibrating flexible cylinder, especially at the middle section. At $z/D = 2$ or 10, the 2P mode changes into a 2S mode with a single vortex per cycle in the far wake. The transverse spacing between the vortices varies with the variation of response amplitude along the length. At $z/D = 6.0$ (the middle section), the width of the vortex street is largest corresponding to the largest transverse response of the cylinder.

Moreover, the time histories of the time-averaged force coefficients and the spectral analysis for instantaneous lift force are presented in figure 9. The mean drag coefficient for the flexible cylinder is higher than that of the rigid cylinder. In contrast, the peak-to-peak value of the lift coefficient for the flexible cylinder is smaller than that of the rigid cylinder. The increase of drag coefficient is probably due to the increase for projected area of the flexible cylinder in one vibrating period, while the decrease for peak-to-peak value of the lift coefficient would be attributed to the different flow patterns along the span (referring to

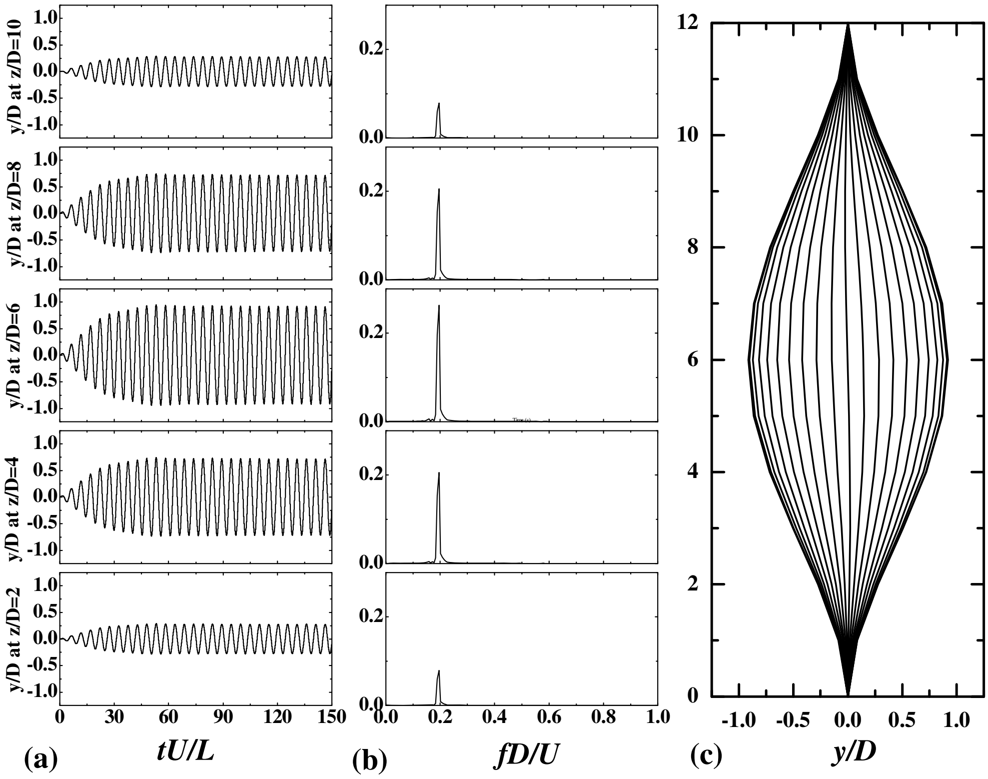

Figure 6. Dynamic response of a flexible cylinder: (a) instantaneous non-dimensional cross-flow displacements, (b) spectra analysis of (a) and (c) cross-flow motion.

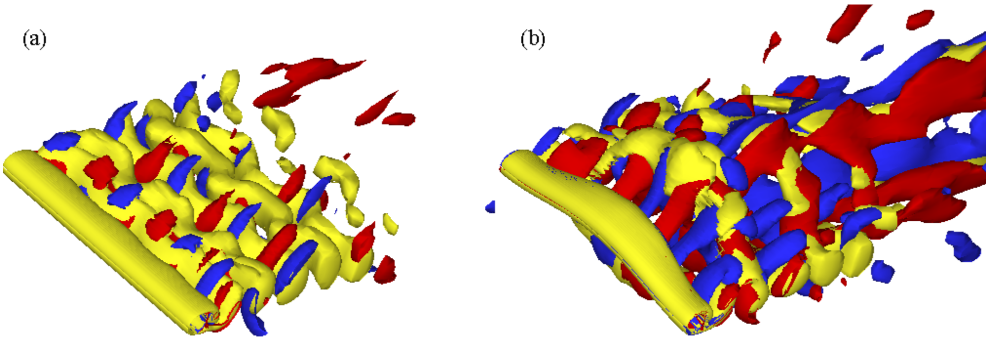

Figure 7. Three-dimensional vortex structure for two cases: (a) rigid cylinder and (b) flexible cylinder.

figure 8) and the poor correlation along the span. From the spectrum analysis in figure 9, it is found that one peak value exists for either a rigid cylinder or a flexible cylinder. The frequency peak (0.189) in the flexible cylinder is near the excited structural frequency (0.195). The counterpart for the rigid cylinder is related to the natural vortex-shedding frequency (0.2167). It is found that the vortex-shedding frequency of the vibrating cylinder is closer to the excited structural frequency, indicating that the structure's natural frequency dominates the vibration as well as the flow wake.

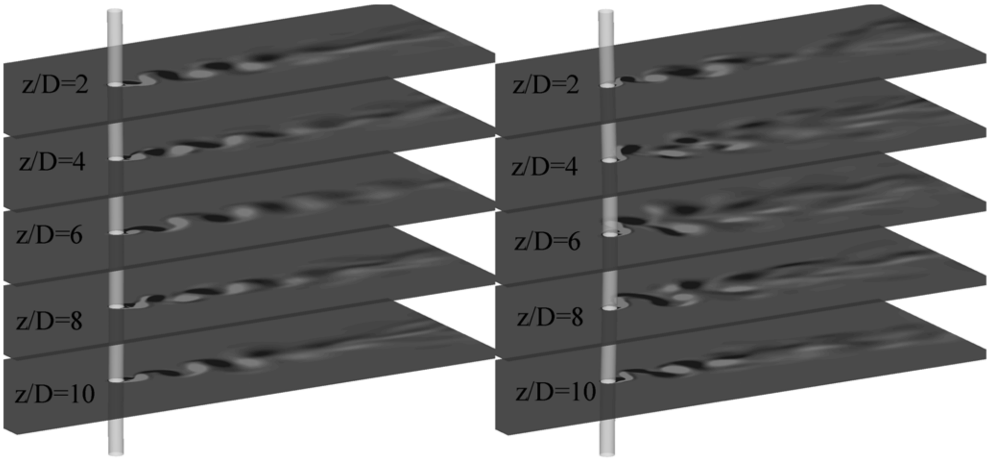

Figure 8. Instantaneous vorticity contours at different z-positions: (a) rigid cylinder and (b) flexible cylinder.

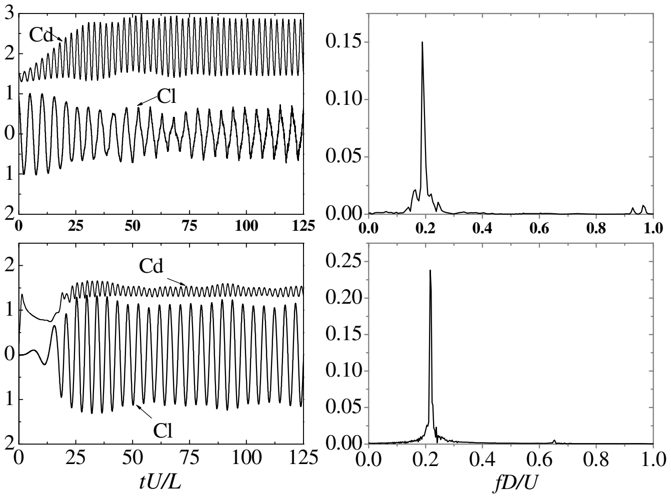

Figure 9. Time histories of force coefficients (left) and the corresponding spectra (right) for two cases: the flexible cylinder (top) and the rigid cylinder (bottom).

3.2.2. Frequency ratio effect. Research on VIV is usually conducted by changing either the reduced velocity (thus Reynolds number) or the frequency ratio. Experimentally, the inflow velocity of the wind or water tunnel can be conveniently changed. Numerically, varying the natural frequency of the structures is preferred. This is also adopted in this paper. As indicated in equation (15), the eigen-frequency of the flexible cylinder is determined by the stiffness (*EI*) under a given mass ratio. With the variation of the stiffness, the structural frequency and thus the ratio of the structural frequency to the vortex-shedding frequency of a rigid cylinder would change. The effect of this change is thus investigated in the following context.

a. Dynamic response

In section 3.2.1, it was shown that the spectra of cylinder displacement at different spanwise positions are identical. Thus $x/Z = 5.0$ is selected to compare the response amplitudes of a cylinder at different frequency ratios. Figures 10 and figure 11 provide the dynamic

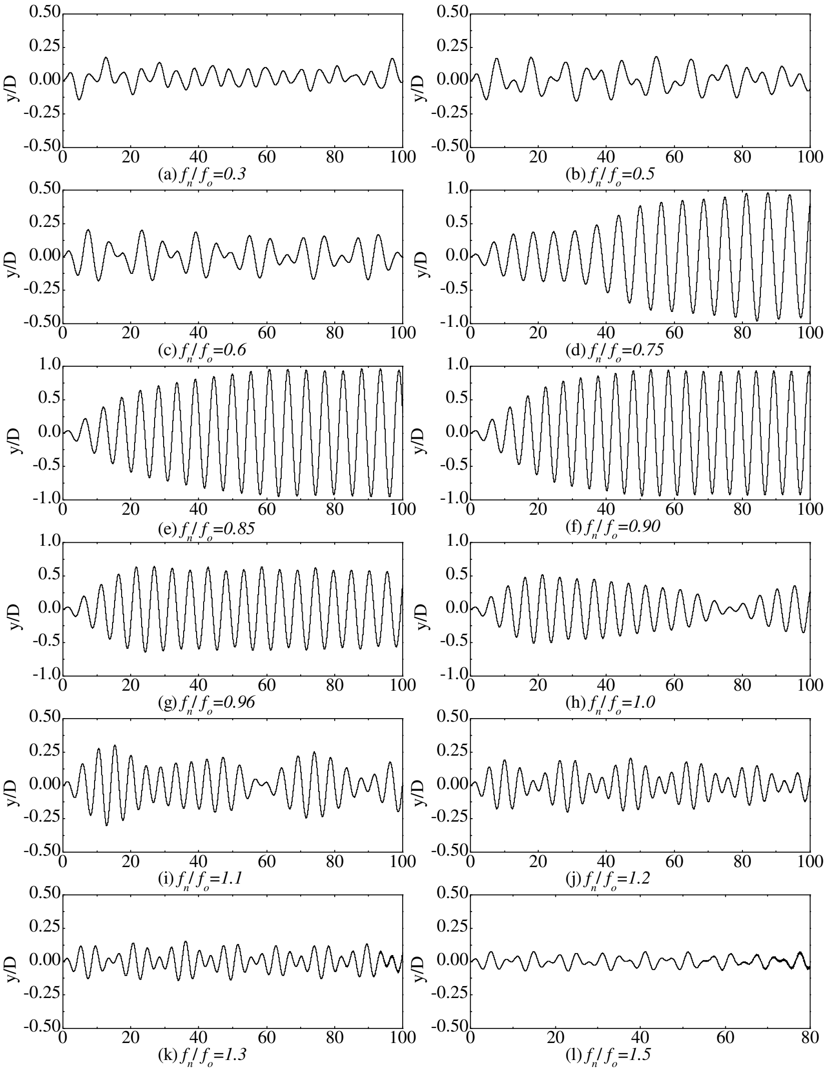

Figure 10. The dynamic response at $Z/D = 5$ for different frequency ratios.

responses and the amplitude spectra analysis at $x/Z = 5.0$ for different frequency ratios. When $0.3 < f_n/f_o < 0.5$, the time history of displacement shows an irregularity, especially at $f_n/f_o = 0.3$, where more than two peak values in the spectra exist. One is smaller than the excited structural frequency and the other is 0.189, which is located between the smaller peak frequency and the excited structural frequency. For $f_n/f_o = 0.75$, the time history of displacement becomes periodic. It is found that there is only one peak and the frequency is also a little smaller than the excited structural frequency. Judging from the spectra and the wake flow patterns, this corresponds to a transition point entering locked-in status. For $0.75 < f_n/f_o < 0.96$, the flow is in synchronization. From figures 10(d)–(g) and figure 11(d)–(g), it is demonstrated that the amplitude peak of spectral analysis is related to the vibrating displacement amplitude. At $f_n/f_o = 0.85$, the displacement shows a maximum value of 1.03, as well as that in spectral analysis. After that, the beating behavior appears and the vibrating

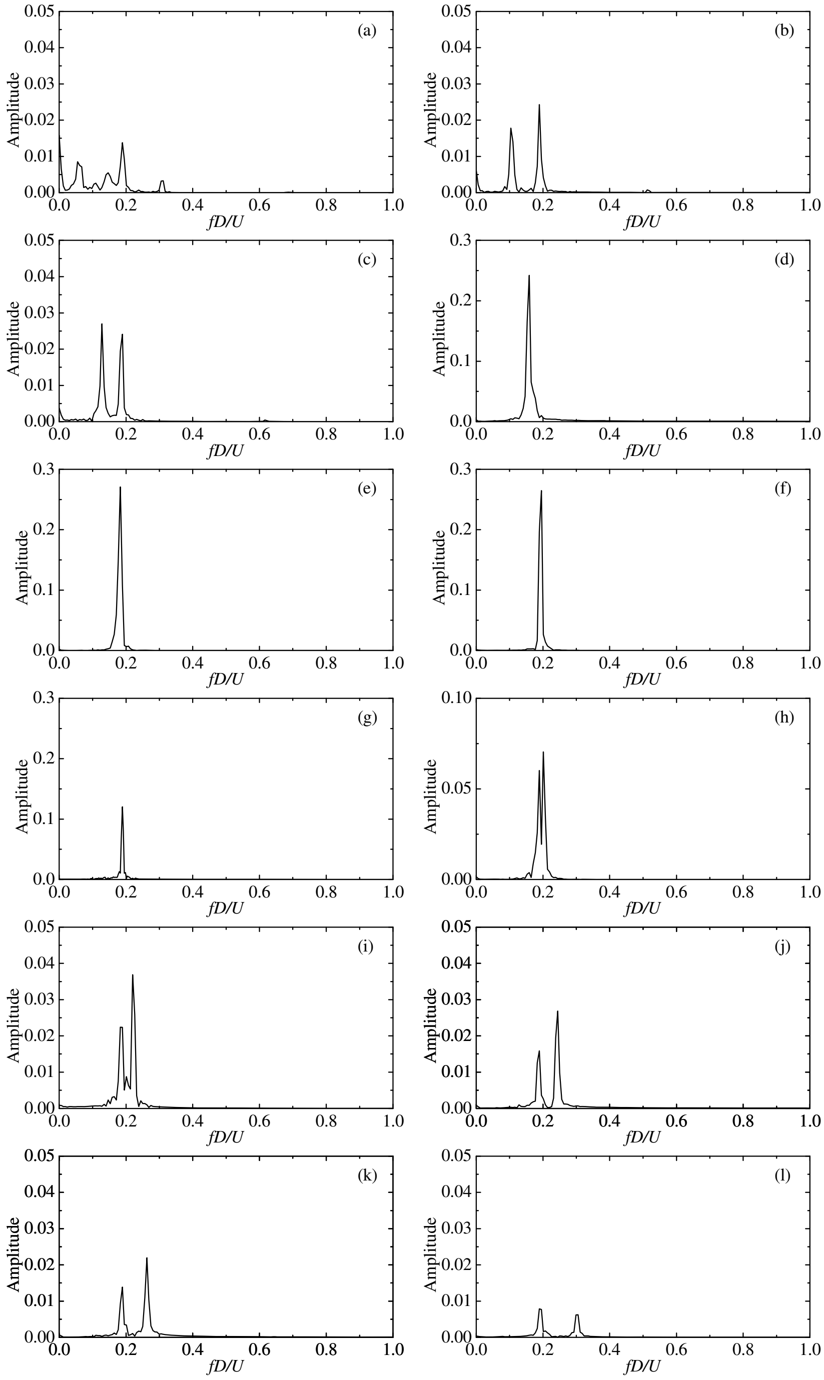

Figure 11. Amplitude spectra of displacement at $Z/D = 5$ for different frequency ratios.

displacement amplitude falls. Two peak frequency values in the spectra appear again and the behavior is the same as that in $0.3 < f_\mathrm{n}/f_\mathrm{o} < 0.5$. It is not surprising that one of the peak frequency values is 0.189, too. We can conclude that the fluid and the structure system

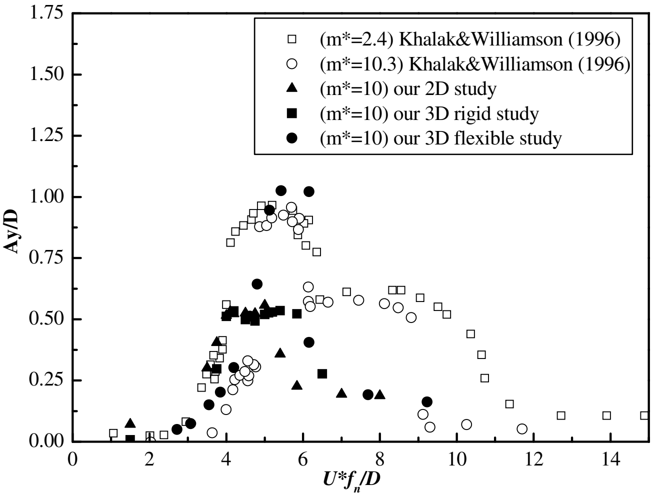

Figure 12. Amplitude of vibrations as a function of the reduced velocity. Compared to experiment results from Khalak and Williamson (1996).

affect each other out of the synchronization and the excited structural frequency dominates the wake flow in the synchronization. However, quantitative explanation for this peak value needs further discussion in near future studies.

The amplitude of vibration as a function of the reduced velocity is exhibited in figure 12. The numerical 3D flexible results are compared to the 2D and 3D rigid results and the experimental results by Khalak and Williamson (1996). There are several differences in parameters between the present study and others. The mass ratios in the experiments are 2.4 and 10.3, while in the present study the mass ratio is 10. The values of the mass damping for the present 2D and 3D rigid results and the previous experimental results are both 0.0013. The experiments were carried out on a rigid cylinder at a high Reynolds number of about 10 000, while our study is based on a low Reynolds number of 1000.

First of all, as the comparison between our 2D results and experimental results reveals, the maximum amplitude in our 2D results is about 0.57D, well below the maximum amplitude of 0.97D found by Khalak and Williamson (1996). The high-amplitude model for the lock-in region is not observed in the 2D results. However, despite the significant differences between 2D simulations and experiments, which have also been observed in Meneghini *et al* (2004), some key phenomena can also be discovered by 2D simulations. As compared to the numerical results of 2D simulations, our 3D rigid results illustrate not too many differences from other available results, with a slightly wider lock-in region range and similar maximum amplitudes that coincide well with the 3D flexible simulation results if $U/f_n^*D > 6.0$. In addition, our 3D flexible simulations present less divergence with the experiments. There are three branches in the 3-D results that match well with the experimental results. The maximum amplitude for $U/f_n^*D = 5.4$ in the 3-D simulations is 1.03D, a little higher than the value of 0.97D for $U/f_n^*D = 5.7$ in experiments at $m^* = 10.3$, where f_n is the excited structural frequency. Good agreement is also reached in the region of the initial branch for our simulations with the experiments. We attribute this difference between our 2D simulations and previous experiments to 3D effect or turbulence. Nevertheless, the difference between the 3D simulations and previous experiments is due to the fact that the circular cylinder in our 3D study is regarded as an Euler–Bernoulli beam but a rigid cylinder in experiments.

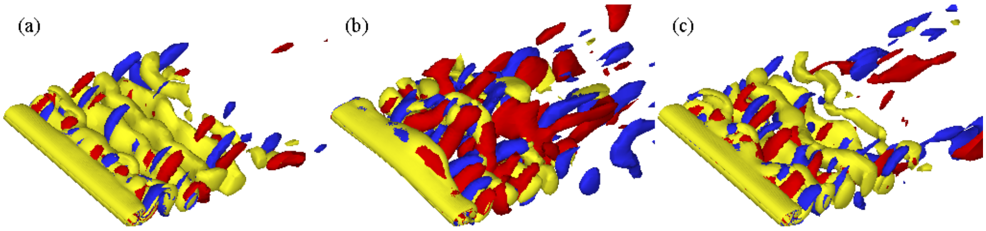

Figure 13. Three-dimensional vortex structure for three typical frequency ratios: (a) $f_n/f_o = 0.6$, (b) $f_n/f_o = 0.85$ and (c) $f_n/f_o = 1.1$.

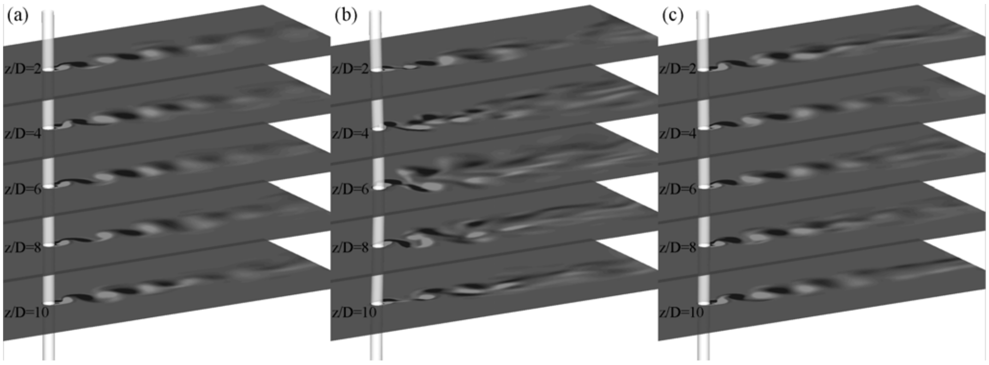

Figure 14. Planar vortical contours at different positions along span-wise direction: (a) $f_n/f_o = 0.6$, (b) $f_n/f_o = 0.85$ and (c) $f_n/f_o = 1.1$.

Except for the tiny divergence discussed above, the amplitude response in our study for the lower branch is below the experimental results. As for the larger reduced velocity, the corresponding structural excited frequency is smaller, so the dynamic response would be distributed in several frequency components, leading to smaller response amplitude compared to the rigid cylinder in experiments. Therefore, the divergence is much more obvious as shown in figure 12 for large reduced velocity. It is noted that the main purpose for figure 12 is not to make a quantitative comparison with experiments, since the limits for the model used in this paper have been discussed above.

b. Three frequency ratios

As the frequency ratio is close to the resonance value, the cylinder vibration begins to affect the vortex pattern in the wake. Comparisons of the vortex pattern for three typical frequency ratios in the wake of a flexible cylinder are presented in figure 13. Figure 14 exhibits the planar vortical contours at different positions along the span-wise direction. These three frequency ratios are 0.6, 0.85 and 1.1, which represent three different branches, i.e. lower branch, upper branch and initial branch, respectively as shown in figure 12. For the frequency ratio of 0.6, the flexible cylinder vibrates at small amplitude and most of the vortex-shedding modes are clearly 2S patterns. This is because at a low frequency ratio, the cylinder behaves more stiffly, which is closer to a rigidly mounted cylinder or a fixed cylinder. However, at a frequency ratio of 0.85, the flexible cylinder vibrates more vigorously and the wake flow is very unstable. The stream-wise vortices can be obviously observed staggering with the span-wise vortex tube. A 2P mode of the vortex pattern can be observed at the planar vortical contours. At a frequency ratio of 1.1, the flexible cylinder returns to its slight vibration state, and the vortex pattern

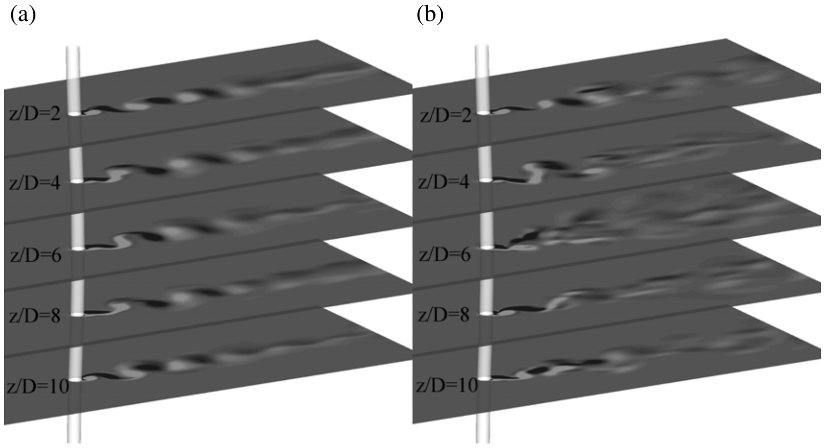

Figure 15. Planar vortical contours at different positions along span-wise direction for $f_n/f_o = 0.75$: (a) $tU/D = 30$ and (b) $tU/D = 100$.

turns back to a 2S mode but at the plane $z/D = 9$, a 2S mode is in the transition to 2P mode and the small vortex in the pair is much weaker than the big one.

From figure 12, it is noted that at $U/f_n^* D = 6.1529$, or $f_n/f_o = 0.75$, there is a jump from the upper branch to the lower branch. This jump can also be observed in figure 10(d), and it is worth analyzing this transition. Figure 15 shows the instantaneous planar vortical vortex patterns at two different time steps: $tU/D = 30$ and $tU/D = 100$. It is apparent that the 2S mode dominates for $tU/D = 30$, while one vortex of the second vortex pair immediately shedding from the cylinder starts to split into two single vortices at $tU/D = 100$. A hybrid pattern combined with 2S mode and 2P mode and some disordered vortex structures appear at different positions along the flexible cylinder. The reason that causes such complicated vortex patterns at this frequency ratio, as well as the unstable wake flow, may be associated with the branch transition and the large amplitude of vibration.

4. Conclusions

In this paper, a numerical simulation of a flexible circular cylinder subjected to VIV is conducted. Conclusions can be drawn as follows:

1. Without a turbulence model, 2D simulations are inadequate to accurately predict the overall flow nature on both the response envelope and the vortex-shedding mechanism, even at relatively low Reynolds numbers.
2. Despite the limits that the beam model holds in this paper, the general trend of the computed amplitude versus reduced velocity curve agrees well with the experimental results for free vibration of a rigid cylinder at low mass-damping.
3. The comparison between a fixed cylinder and a flexible cylinder shows that the vibration significantly altered the three dimensionality in the wake. The stream-wise vortex structures are enhanced especially with large response amplitude cases or within the resonance region.
4. The results for various frequency ratios show that different wake patterns appear according to the various frequency ratios, such as 2S mode, 2P mode and some more complicated modes. The wake pattern would be different at the different sections along

the span-wise length of the cylinder, due to the fact that the two ends of the beam are fixed.

It is worth pointing out that the Reynolds number in the present study is 1000, at which the three dimensionality is expected to be fully developed. Further investigations on such a 3D effect for a flexible cylinder VIV are necessary.

Acknowledgments

The authors acknowledge financial support from the National Natural Science Foundation of China (grant no 10802075), and support from the Fundamental Research Funds for the Central Universities (grant no 2011QNA4023). All numerical computations were performed at the Center for Engineering and Scientific Computation (CESC), Zhejiang University. The authors are grateful for this assistance.

References

Batina J 1990 Unsteady Euler airfoil solutions using unstructured dynamic meshes *AIAA J.* **28** 1381–8
Bearman P W 1984 Vortex shedding from oscillating bluff-bodies *Annu. Rev. Fluid Mech.* **16** 195–222
Brika D and Laneville A 1993 Vortex-induced vibrations of a long flexible circular-cylinder *J. Fluid Mech.* **250** 481–508
Brika D and Laneville A 1995 An Experimental-study of the aeolian vibrations of a flexible circular-cylinder at different incidences *J. Fluids Struct.* **9** 371–91
Brika D and Laneville A 1996 A laboratory investigation of the aeolian power imparted to a conductor using a flexible circular cylinder *IEEE Trans. Power Deliv.* **11** 1145–52
Demirdzic I and Peric M 1988 Space conservation law in finite volume calculations of fluid-flow *Int. J. Numer. Methods Fluids* **8** 1037–50
Deng J, Ren -L and Chen W 2005 Numerical simulation of flow-induced vibration on two circular cylinders in tandem arrangment *J. Hydrodyn.* B **17** 60–66
Deng J, Ren A-L and Shao X-M 2007 The flow between a stationary cylinder and a downstream elastic cylinder in cruciform arrangement *J. Fluids Struct.* **23** 715–31
Evangelinos C and Karniadakis G E M 1999 Dynamics and flow structures in the turbulent wake of rigid and flexible cylinders subject to vortex-induced vibrations *J. Fluid Mech.* **400** 91–124
Feng C C 1968 The measurements of vortex-induced effects in flow past a stationary and oscillating circular and D-section cylinders *Master's Thesis* University of British Columbia
Ferziger J and Peric M 1995 *Computational methods for fluid dynamics* (Berlin: Springer)
Flemming F and Williamson C H K 2005 Vortex-induced vibrations of a pivoted cylinder *J. Fluid Mech.* **522** 215–52
Fujarra A L C, Pesce C P, Flemming F and Williamson C H K 2001 Vortex-induced vibration of a flexible cantilever *J. Fluids Struct.* **15** 651–8
Gabbai R D and Benaroya H 2005 An overview of modeling and experiments of vortex-induced vibration of circular cylinders *J. Sound Vib.* **282** 575–616
Govardhan R and Williamson C H K 2000 Modes of vortex formation and frequency response of a freely vibrating cylinder *J. Fluid Mech.* **420** 85–130
Griffin O M 1992 Vortex-induced vibrations of marine structures in uniform and sheared currents *Technical Report NSF Workshop on Riser Dynamics* University of Michigan
Huang K, Chen H C and Chen C R 2010 Vertical riser VIV simulation in uniform current *J. Offshore Mech. Arctic Eng.-Trans. ASME* **132** 031101
Huera-Huarte F J and Bearman P W 2009a Wake structures and vortex-induced vibrations of along flexible cylinder. Part 1. Dynamic response *J. Fluids Struct.* **25** 969–90
Huera-Huarte F J and Bearman P W 2009b Wake structures and vortex-induced vibrations of along flexible cylinder. Part 2. Drag coefficients and vortex modes *J. Fluids Struct.* **25** 991–1006
Huera-Huarte F J, Bearman P W and Chaplin J R 2006 On the force distribution along the axis of a flexible circular cylinder undergoing multi-mode vortex-induced vibrations *J. Fluids Struct.* **22** 897–903
Issa R I 1986 Solution of the implicitly discretized fluid-flow equations by operator-splitting *J. Comput. Phys.* **62** 40–65

Jasak H and Tukovic Z 2007 Auto Mesh motion for the unstructured finite volume method *Trans. FAMENA* **30** 1–18

Jeong J and Hussain F 1995 On the identification of a vortex *J. Fluid Mech.* **285** 69–94

Khalak A and Williamson C H K 1996 Dynamics of a hydroelastic cylinder with very low mass and damping *J. Fluids Struct.* **10** 455

Khalak A and Williamson C H K 1997a Dynamics of a hydroelastic cylinder with very low mass and damping - Response *J. Fluids Struct.* **11** 551–52

Khalak A and Williamson C H K 1997b Fluid forces and dynamics of a hydroelastic structure with very low mass and damping *J. Fluids Struct.* **11** 973–82

Khalak A and Williamson C H K 1999 Motions, forces and mode transitions in vortex-induced vibrations at low mass-damping *J. Fluids Struct.* **13** 813–51

Lee L and Allen D 2010 Vibration frequency and lock-in bandwidth of tensioned, flexible cylinders experiencing vortex shedding *J. Fluids Struct.* **26** 602–10

Meneghini J R, Saltara F, Fregonesi R D, Yamamoto C T, Casaprima E and Ferrari J A 2004 Numerical simulations of VIV on long flexible cylinders immersed in complex flow fields *Eur. J. Mech.* B **23** 51–63

Newman D and Karniadakis G E 1996 Simulations of flow over a flexible cable: A comparison of forced and flow-induced vibration *J. Fluids Struct.* **10** 439

Newman D J and Karniadakis G E 1997 A direct numerical simulation study of flow past a freely vibrating cable *J. Fluid Mech.* **344** 95–136

Pesce C P and Fujarra A L C 2000 Vortex-induced vibrations and jump phenomenon: Experiments with a clamped flexible cylinder in water *Int. J. Offshore Polar Eng.* **10** 26–33

Sarpkaya T 2004 A critical review of the intrinsic nature of vortex-induced vibrations *J. Fluids Struct.* **19** 389–447

Schulz K W and Kallinderis Y 1998 Unsteady flow structure interaction for incompressible flows using deformable hybrid grids *J. Comput. Phys.* **143** 569–97

Willamson C H K and Roshko A 1988 Vortex formation in the wake of an oscillating cylinder *J. Fluids Struct.* **2** 355–81

Williamson C H K and Govardhan R 2004 Vortex-induced vibrations *Annu. Rev. Fluid Mech.* **36** 413–55

Williamson C H K and Govardhan R 2008 A brief review of recent results in vortex-induced vibrations *J. Wind Eng. Ind. Aerodyn.* **96** 713–35

Xu J, He M and Bose N 2009 Vortex modes and vortex-induced vibration of a long, flexible riser *Ocean Eng.* **36** 456–67

Yamamoto C T, Meneghini J R, Saltara F, Fregonesi R A and Ferrari J A 2004 Numerical simulations of vortex-induced vibration on flexible cylinders *J. Fluids Struct.* **19** 467–89